

Quantum Monte Carlo study of semiconductor artificial graphene nanostructures

Gökhan Öztarhan , E. Bulut Kul , Emre Okcu , and A. D. Güçlü 
Department of Physics, İzmir Institute of Technology, 35430 Urla, İzmir, Turkey

 (Received 31 October 2022; revised 3 October 2023; accepted 12 October 2023; published 30 October 2023)

Semiconductor artificial graphene nanostructures where the Hubbard model parameter U/t can be of the order of 100, provide a highly controllable platform to study strongly correlated quantum many-particle phases. We use accurate variational and diffusion Monte Carlo methods to demonstrate a transition from antiferromagnetic to metallic phases for an experimentally accessible lattice constant $a = 50$ nm in terms of lattice site radius ρ , for finite-sized artificial honeycomb structures nanopatterned on GaAs quantum wells containing up to 114 electrons. By analyzing spin-spin correlation functions for hexagonal flakes with armchair edges and triangular flakes with zigzag edges, we show that edge type, geometry, and charge nonuniformity affect the steepness and the crossover ρ value of the phase transition. For triangular structures, the metal-insulator transition is accompanied with a smoother edge polarization transition.

DOI: [10.1103/PhysRevB.108.L161114](https://doi.org/10.1103/PhysRevB.108.L161114)

In recent years, technological advances in photonic and condensed-matter-based artificial superlattices give us opportunities to develop practical quantum simulators [1–14]. These quantum simulators allow us to replicate complex systems that are hard to fabricate and provide us with a playground to verify theoretical predictions. In this respect, artificial graphene (AG) nanostructures, designed by imitating the two-dimensional (2D) honeycomb pattern of graphene, have been proven to be good candidates for being reliable and controllable sources for both the fabrication and investigation of many physical phenomena related to Dirac fermions [13–19]. In particular, AG nanostructures can be formed using semiconductor materials. While earlier reports on nanopatterned artificial graphene on GaAs quantum well (QW) structures found no evidence of massless Dirac fermions (MDFs), presumably because of the relatively large lattice periods [20–22], in recent experimental works using modulation-doped AlGaAs/GaAs quantum wells [13,14], shrinking down of the lattice constant of the honeycomb array to approximately 50 nm allowed the observation of the predicted graphenelike behavior [21,23–25].

The observation of Dirac fermions in AG also opens up a fresh way of studying graphene quantum dots [26] where geometry, size, and edge type is expected to give rise to several physical properties such as band-gap opening [27], edge magnetization [28–30], and optical control [31]. However, the fabrication and reliability issues such as edge reconstruction or the presence of impurities, make it harder to observe interesting phenomena predicted to occur in nanostructured graphene. Semiconductor AG nanostructures, on the other hand, offer several advantages such as the tunability of system parameters including the lattice constant, site radius, and potential depth, which, in turn, allow the control of electron-electron interactions and tunneling strength between sites, in particular the Hubbard parameter U/t . In experimental structures with a lattice constant $a = 50$ nm [14], U/t can be as high as 350 (as we will argue below), i.e., two orders of magnitude larger than the critical value for the antiferromag-

netic Mott transition predicted by calculations based on the Hubbard model for a honeycomb lattice [32–35]. Moreover, unlike in real graphene, long-range electron repulsion does not cancel the attraction of the artificial confining potential in AG even near charge neutrality. For such large and long-ranged electron interactions, a nonperturbative many-body approach is desirable for the careful treatment of correlation effects.

Earlier theoretical work on electron interaction effects in semiconductor AG nanostructures based on density functional theory (DFT) showed that Dirac bands were stable against interactions [23,24], which was also confirmed using path integral Monte Carlo calculations [25]. However, recent calculations using Hartree-Fock and exact diagonalization approaches for a triangular zigzag geometry with $a = 12.5$ – 15 nm show that a transition from an antiferromagnetic (AFM) insulator to metallic phases occurs, pointing to the importance of electron interactions [36].

In this Letter, we use continuum variational Monte Carlo (VMC) and diffusion Monte Carlo (DMC) methods for the nonperturbative and accurate treatment of many-body correlations within the fixed-node approximation to study GaAs-based AG nanostructures. First, we consider a hexagonal armchair geometry which serves as a bridge between the finite-size samples and bulk graphene [27], with a lattice constant $a = 50$ nm following recent experimental work [14]. We show that a transition from AFM to metallic phase occurs, but is affected by a nonuniform charge distribution in the sample due to finite-size effects. This charge nonuniformity, which is not present in real graphene quantum dots, causes the phase transition to be steeper and to occur at a smaller value of ρ . We also investigate AG quantum dots with triangular zigzag geometry and show that edge magnetization survives the phase transition, in agreement with a previous theoretical prediction for smaller lattice constants [36].

Our model of nanostructured semiconductor AG consists of N interacting electrons in a honeycomb array of N confining potentials, described by the many-body

Hamiltonian

$$H = -\frac{1}{2} \sum_i \nabla_i^2 + \sum_i V(\mathbf{r}_i) + \sum_i k|\mathbf{r}_i|^2 + \sum_{i<j} \frac{1}{r_{ij}}, \quad (1)$$

in effective atomic units (electronic charge e , dielectric constant ϵ , effective mass m^* , and \hbar are set to 1), where $1/r_{ij}$ is the Coulomb interaction between the electrons, $V(\mathbf{r}_i)$ is the total potential energy of the confining potentials, and k is the spring constant of the quadratic gate potential located at the center of the system which controls the finite-size effects. Typical material properties for GaAs, an effective electron mass $m^* = 0.067m_0$ and dielectric constant $\epsilon = 12.4$, are used. The corresponding effective Bohr radius is $a_0^* = 9.794$ nm, and the effective Hartree energy is 11.857 meV. The honeycomb array of potential wells is modeled using Gaussian-like functions [25],

$$V(\mathbf{r}) = V_0 \sum_{\mathbf{R}_0} \exp[-(|\mathbf{r} - \mathbf{R}_0|^2/\rho^2)^s], \quad (2)$$

where $s \geq 1$, V_0 is the potential depth, ρ is the radius, and s is the sharpness of the potential wells. \mathbf{R}_0 is the location of the potential wells. In our numerical calculations, the dot-to-dot distance (lattice constant) was fixed to $a = 50$ nm, while several radius values from $\rho = 10$ to 35 nm were covered. Three different sharpness values were used: $s = 1$ for a Gaussian potential, $s = 2.8$ for a sharp, muffin-tin-like potential, and $s = 1.4$ in between. V_0 values vary depending on dot radius (e.g., increasing monotonically with the dot radius, from -38 to -15 meV for $s = 1.4$ and $N = 42$), tuned to keep the total energy of the system close to zero, since our aim is to imitate the charge neutral behavior of finite-sized graphene quantum dots. For too high values of V_0 , electrons tend to escape the system during VMC or DMC simulations, while for too low values overlocalization occurs [21].

The accuracy of the numerical calculations depends on the trial wave functions in both VMC and DMC methods. One starts with a set of single-particle orbitals (e.g., localized Gaussians or from self-consistent calculations) to build a Slater-Jastrow trial wave function $\Psi_T(\mathbf{R})$ which is a linear combination of products of up- and down-spin Slater determinants of these orbitals multiplied by a Jastrow factor (the details of our Jastrow factor is given in Ref. [37]). After the VMC calculations where Jastrow parameters as well as the Gaussian functions' width are optimized using an energy minimization technique [38], we use fixed-node DMC [39,40] to project the optimized many-body wave function onto a better approximation of the true ground state, an approximation that has the same nodes as $\Psi_T(\mathbf{R})$. The resulting fixed-node DMC energy is an upper bound to the true energy and depends only on the nodal structure of the Slater part of the trial wave function $\Psi_T(\mathbf{R})$ [39].

In order to form Slater determinants, we prepare three different types of orbitals aiming to capture metallic or AFM insulator phases, depending on the potential well radius ρ : (i) Localized Gaussian functions are proven to be one of the most suitable functions for 2D systems of quantum dots [37,41,42] and are expected to provide a better description of strongly localized states. (ii) Tight-binding (TB) orbitals, at the other extreme, may be used to describe metallic phases in

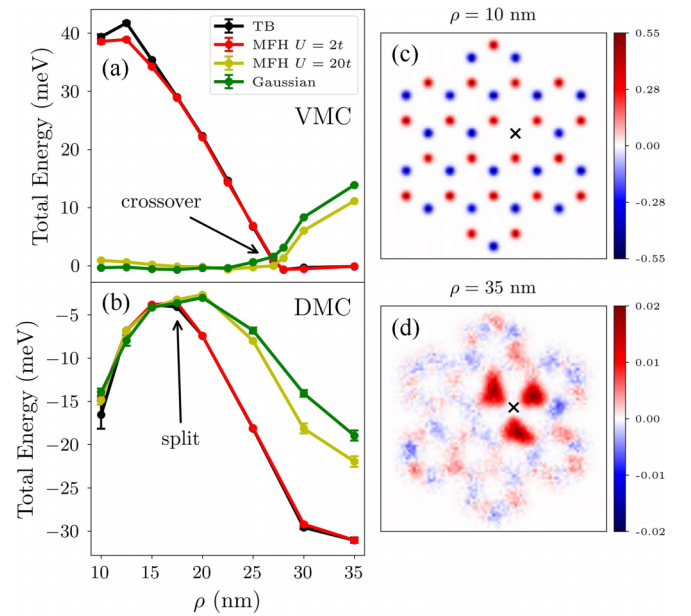


FIG. 1. Armchair hexagonal flake results, $s = 1.4$, $k = 0$, and $N = 42$, plotted for several trial wave functions. (a) VMC total energy vs ρ . (b) DMC total energy vs ρ . (c) Extrapolated pair spin density results for $\rho = 10$ nm, using a tight-binding trial wave function. (d) Extrapolated pair spin density results for $\rho = 35$ nm, using a tight-binding trial wave function. The reference electron is located at the point marked by an \times for (c) and (d).

which electrons move more freely. (iii) Mean-field Hubbard (MFH) orbitals can describe both localized and liquidlike states depending on the ratio U/t . Corresponding variational and fixed-node energies of those three types of orbitals are expected to suggest a possible transition from a metallic state to an AFM order as a function of ρ . In this work, all quantities that do not commute with the Hamiltonian were calculated using an extrapolated estimator, $\langle \hat{O} \rangle = 2\langle \hat{O} \rangle_{\text{DMC}} - \langle \hat{O} \rangle_{\text{VMC}}$ [39].

Figure 1(a) shows the VMC energies obtained from TB, MFH, and Gaussian orbitals, as a function of ρ , for an armchair hexagonal geometry with 42 sites and 42 electrons. The parabolic gate potential parameter is turned off ($k = 0$) and its effect will be discussed in a later section. At low ρ , Gaussian and MFH $U = 20t$ orbitals provide better variational energies. As ρ is increased to ≈ 27 nm, a clear crossover (from an insulator to metallic phase) occurs above which TB and MFH $U = 2t$ orbitals take the lead. Fixed-node DMC energies, however, reveal a somewhat different picture, shown in Fig. 1(b). From $\rho = 10$ nm to $\rho \approx 18$ nm, all trial wave functions give similar energies within the statistical error bars, and split near $\rho \approx 18$ nm. After the split, the ground state of the system is represented by TB and MFH $U = 2t$ trial wave functions. These results show that, surprisingly, the TB trial wave function has an equally good nodal structure as the Gaussian orbitals at low ρ values, raising questions about the true nature of the ground state. To reveal the underlying electronic and magnetic structure, we consider the pair densities $p_{\sigma\sigma_0}(\mathbf{r}, \mathbf{r}_0)$, the probability of finding an electron with spin σ at location \mathbf{r} when an electron with spin σ_0 is fixed at location \mathbf{r}_0 , and the pair spin densities, $p_{\uparrow\downarrow}(\mathbf{r}, \mathbf{r}_0) - p_{\downarrow\uparrow}(\mathbf{r}, \mathbf{r}_0)$. Figures 1(c) and

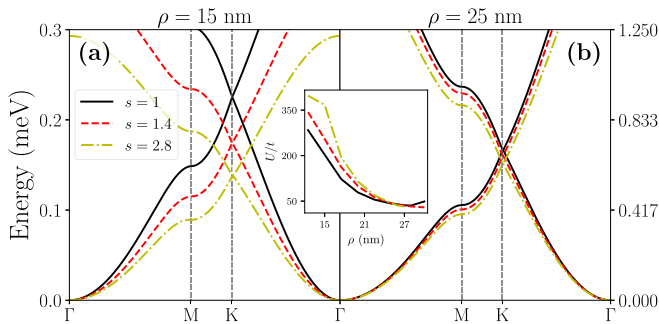


FIG. 2. DFT band structure of bulk artificial graphene for (a) $\rho = 15$ nm and (b) $\rho = 25$ nm. The inset figure shows the U/t ratio plotted against dot radius ρ , predicted by DFT and single-particle calculations.

1(d) show the pair spin densities for a reference spin-down electron fixed on top of a site (chosen to break the system symmetry and away from the edges) shown with a cross (\times). At $\rho = 10$ nm, electrons are well localized at the sites, leading to an AFM insulator. On the other hand, at large values of ρ , spin-spin correlations are weak and short ranged up to nearest neighbors. While these results confirm that a transition from an AFM insulator to a metallic phase does occur as observed in previous work [36], there are several issues left to address: (i) an inconsistent signature regarding the crossover ρ value obtained from VMC and DMC energies and the underlying dynamics of the transition, (ii) finite-size and edge effects, and (iii) the relationship to bulk properties.

Now, we turn our attention to the 2D bulk properties for similar system parameters used in our calculations. As mentioned earlier, V_0 values are tuned to keep the total energy of the system close to zero. The question is whether such a set of parameters leaves the Dirac cone structure intact, which may otherwise have repercussions on electronic and magnetic properties. In Fig. 2, we show the results of our DFT calculations in the local density approximation (LDA). The Dirac cone structure is preserved for the range $\rho = [12.5, 30]$ nm; outside this range the Dirac fermion picture becomes distorted. Moreover, we can estimate the TB hopping parameter t from the slope of the Dirac cones as $t = \frac{2}{3}a^{-1}dE/dk$, where a is the lattice constant. As we see from Fig. 2, t increases with increasing ρ but decreasing s , as expected. In addition to t , to build a Hubbard model, we estimated the U value for a single well using $U = 2\pi \int rn(r)V_e(r)dr$ after solving the single-particle Schrödinger equation. In the inset of Fig. 2, we plot U/t as a function of ρ which shows a fast decay from ≈ 300 to 50 between $\rho = 15$ and 20. Surprisingly, these results indicate that the critical U/t value for a metal-insulator transition in AG is much higher than the critical value of ~ 3.8 predicted by Hubbard calculations [32–35], presumably due to the importance of long-range interactions and deviation from the nearest-neighbor TB approximation as ρ increases. On the other hand, according to our quantum Monte Carlo (QMC) calculations, MFH trial wave functions based on the LDA estimation of U/t do not provide the most suitable fixed-node energies, and the nodal structure of the simplest TB trial wave functions works best for the whole range of

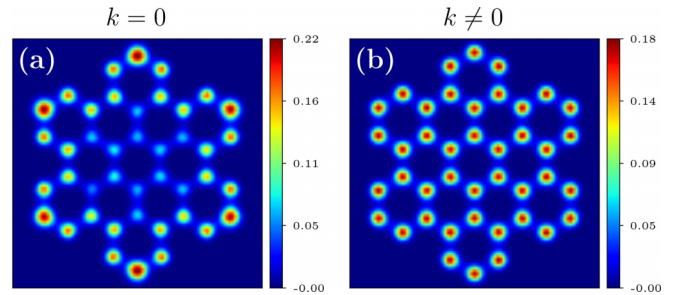


FIG. 3. Effect of k on total electron densities for an armchair hexagonal flake. $s = 1.4$, $\rho = 25$ nm, and $N = 42$ using a tight-binding trial wave function. (a) $k = 0$. (b) $k = 3.56 \times 10^{-4}$ meV/nm².

system parameters regardless of the underlying electronic or magnetic state.

Next, we focus on finite-size effects. While V_0 is tuned to imitate the overall charge neutrality, long-range electron interactions still affect the charge distribution inside the system, pushing the electrons towards the edges and/or corners, as can be seen in Fig. 3(a) for the hexagonal armchair system with $N = 42$, $s = 1.4$, and $\rho = 25$ nm. While, in principle, V_0 can be decreased further to achieve charge uniformity, this would localize the electrons too strongly to their sites and make the system negatively charged unlike in real graphene systems. An alternative solution is to apply a quadratic gate potential controlled by the parameter k in Eq. (1). When $k > 0$, a quadratic gate potential attracts the electrons towards the center of the system so that the charge uniformity is preserved, and finite-size effects are minimized, as shown in Fig. 3(b) for $k = 3.56 \times 10^{-4}$ meV/nm².

In order to understand in more detail the dynamics of the transition from an AFM insulator to metallic phase including effects of charge nonuniformity and quantum well potential sharpness, we consider a real-space spin-spin correlation function g normalized by the density-density correlations, $g = \langle s_i s_j \rangle / \langle n_i n_j \rangle$, where s_i and n_i are the average total spin and total electron densities on site i within a radius r , and i, j are the nearest-neighbor sites. We used $r = a/2$ in all spin-spin correlation calculations, where a is the lattice constant. The output values of the function remain in the $[-1, 1]$ range, with $g = -1$ corresponding to AFM and $g = 0$ corresponding to the metallic configuration ($g = 1$ means that all spins are in the same direction, which does not happen in the subspace $S_z = 0$ considered here). In Fig. 4(a), g is plotted against ρ obtained from different trial wave functions, for $s = 1.4$ and $k = 3.56 \times 10^{-4}$ meV/nm² to obtain charge uniformity. We have also added a weighted average of all trial wave functions using the Boltzmann distribution at $T = 4$ K, representing the ground state, to ensure that no effects are missed when various trial wave functions lead to the same ground-state energies within statistical noise. The emerging picture is that the system remains strongly AFM between $\rho = 10$ and 18 nm, then starts fading smoothly, finally reaching a fully metallic regime around $\rho = 30$ nm. We note that the DMC energies for $k > 0$ split around $\rho = 26$ nm [see the inset of Fig. 4(a)], in contrast with the $k = 0$ results in Fig. 1(b) where the split occurs near

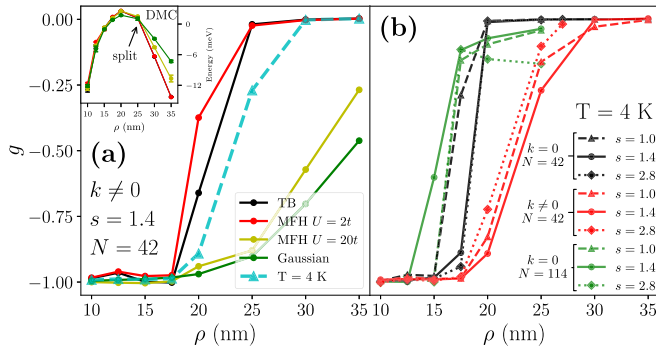


FIG. 4. Armchair hexagonal flake results. (a) Extrapolated spin-spin correlation function for $s = 1.4$, $k = 3.56 \times 10^{-4}$ meV/nm², and $N = 42$. The inset in (a) shows DMC energy results shifted by a constant value. (b) Extrapolated spin-spin correlation function weight averaged at $T = 4$ K plotted for several k , s , and flake sizes.

$\rho = 18$ nm. Figure 4(b) summarizes all weight-averaged g values obtained for different k and s values, and for both flake sizes. Interestingly, for $k = 0$ the transition from an AFM to metallic regime is sharper than for charge uniform systems ($k > 0$), albeit at lower ρ values. Sharpness s and system size N , on the other hand, do not have a significant effect on the transitions.

For triangular zigzag structures, spin-polarized edges even in the metallic phase are expected due to the imbalance between the two sublattices [28–30,36,43], with a nonzero ground-state total spin $S_z = (N_A - N_B)/2$, where N_A and N_B are the number of A and B sublattice atoms, according to Lieb’s theorem [44]. In our AG flake, the total spin is $S_z = 2$ for $N = 46$ and $S_z = 5/2$ for $N = 61$. An analysis of the spin-spin correlation functions for $s = 1.4$ and $k = 2.7 \times 10^{-4}$ meV/nm² leads to a similar picture as before; the system with $N = 46$ sites is perfectly AFM between $\rho = 10$ and 20 nm, then smoothly vanishes between $\rho = 20$ and 35 nm, before becoming completely metallic. For $N = 61$ sites, although the transition is not as smooth presumably due to larger statistical fluctuations at a large system size, a similar picture emerges [Fig. 5(c)]. In order to understand the edge magnetization during the transition, we consider an edge polarization ratio defined as

$$p_r = \frac{\langle |s_{i \in \text{edge}}| \rangle - \langle |s_{i \in \text{bulk}}| \rangle}{\langle |s_{i \in \text{edge}}| \rangle + \langle |s_{i \in \text{bulk}}| \rangle}, \quad (3)$$

which gives one if only edge sites are polarized, and zero if edge and bulk sites are equally (un)polarized. In Fig. 5(b), the edge polarization ratio increases as ρ increases, indicating that spins are polarized more at the edges as the system goes into a metallic phase similar to real triangular zigzag graphene quantum dots, and consistent with the spin density results in the insets of Figs. 5(b) and 5(d), demonstrating a metallic phase with edge-polarized spins at $\rho = 35$ nm for 46 sites and at $\rho = 30$ nm for 61 sites. Additionally, in Fig. 5, the weighted average analysis also confirms that the triangular zigzag AG flake undergoes a metal-insulator transition between ~ 18 and 30 nm dot radius. However, the edge polarization transition occurs slower compared to the metal-insulator transition.

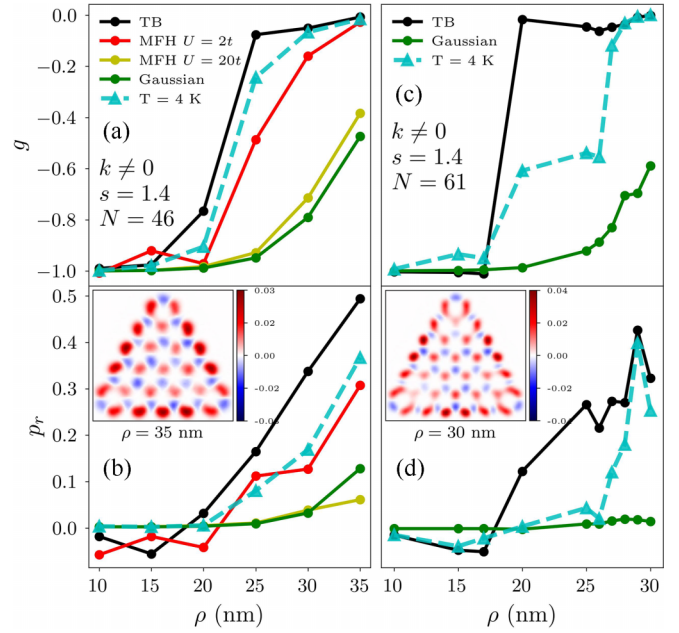


FIG. 5. Triangular flake with zigzag edge results, $s = 1.4$ and $k = 2.7 \times 10^{-4}$ meV/nm², plotted for several trial wave functions and different flake sizes. (a), (c) Extrapolated spin-spin correlation function for 46 and 61 sites. (b), (d) Extrapolated edge polarization function for 46 and 61 sites. Inset of (b): Extrapolated spin density results for $\rho = 35$ nm, $N = 46$, using a tight-binding trial wave function. Inset of (d): Extrapolated spin density results for $\rho = 30$ nm, $N = 61$, using a tight-binding trial wave function.

In summary, we have shown that a metal-antiferromagnetic insulator transition occurs in nanopatterned GaAs-based artificial graphene structures including up to $N = 114$ electrons with a lattice constant $a = 50$ nm as a function of site radius, using accurate variational and diffusion Monte Carlo methods, within the Dirac regime as confirmed by our density functional calculations. Our approach, where a simple tight-binding trial wave function combined with a Jastrow factor is found to be sufficient to account for electron correlation effects in both metallic and antiferromagnetic regimes, allows direct modeling of system parameters, making it possible to systematically investigate the effects of edge type, geometry, size, quantum well shape, and gate potentials. We have shown that the steepness and the crossover ρ value of the phase transition is affected by charge nonuniformity due to finite-size effects. For triangular structures exhibiting magnetized edge states, the edge polarization transition is shown to occur more slowly compared to the metal-insulator transition.

We thank C. J. Umrigar for his endless support for the CHAMP [45] program with which our QMC simulations have been performed, and Pawel Hawrylak and Yasser Saleem for valuable conversations. This work was supported by The Scientific and Technological Research Council of Turkey (TUBITAK) under the 1001 Grant Project No. 119F119. The numerical calculations reported in this study were partially performed at TUBITAK ULAKBIM, High Performance and Grid Computing Center (TRUBA resources).

- [1] I. Bloch, *Nat. Phys.* **1**, 23 (2005).
- [2] A. Mazurenko, C. S. Chiu, G. Ji, M. F. Parsons, M. Kanász-Nagy, R. Schmidt, F. Grusdt, E. Demler, D. Greif, and M. Greiner, *Nature (London)* **545**, 462 (2017).
- [3] I. Buluta and F. Nori, *Science* **326**, 108 (2009).
- [4] S. Kuhr, *Natl. Sci. Rev.* **3**, 170 (2016).
- [5] H. Weimer, M. Müller, I. Lesanovsky, P. Zoller, and H. P. Büchler, *Nat. Phys.* **6**, 382 (2010).
- [6] R. Islam, E. E. Edwards, K. Kim, S. Korenblit, C. Noh, H. Carmichael, G.-D. Lin, L.-M. Duan, C.-C. J. Wang, J. K. Freericks *et al.*, *Nat. Commun.* **2**, 377 (2011).
- [7] J. Salfi, J. A. Mol, R. Rahman, G. Klimeck, M. Y. Simmons, L. C. L. Hollenberg, and S. Rogge, *Nat. Commun.* **7**, 11342 (2016).
- [8] C. Hempel, C. Maier, J. Romero, J. McClean, T. Monz, H. Shen, P. Jurcevic, B. P. Lanyon, P. Love, R. Babbush *et al.*, *Phys. Rev. X* **8**, 031022 (2018).
- [9] A. Aspuru-Guzik and P. Walther, *Nat. Phys.* **8**, 285 (2012).
- [10] J. Cai, A. Retzker, F. Jelezko, and M. B. Plenio, *Nat. Phys.* **9**, 168 (2013).
- [11] H. Bernien, S. Schwartz, A. Keesling, H. Levine, A. Omran, H. Pichler, S. Choi, A. S. Zibrov, M. Endres, M. Greiner *et al.*, *Nature (London)* **551**, 579 (2017).
- [12] T. Li, S. Jiang, L. Li, Y. Zhang, K. Kang, J. Zhu, K. Watanabe, T. Taniguchi, D. Chowdhury, L. Fu *et al.*, *Nature (London)* **597**, 350 (2021).
- [13] L. Du, S. Wang, D. Scarabelli, L. N. Pfeiffer, K. W. West, S. Fallahi, G. C. Gardner, M. J. Manfra, V. Pellegrini, S. J. Wind *et al.*, *Nat. Commun.* **9**, 3299 (2018).
- [14] S. Wang, D. Scarabelli, L. Du, Y. Y. Kuznetsova, L. N. Pfeiffer, K. W. West, G. C. Gardner, M. J. Manfra, V. Pellegrini, S. J. Wind *et al.*, *Nat. Nanotechnol.* **13**, 29 (2018).
- [15] K. K. Gomes, W. Mar, W. Ko, F. Guinea, and H. C. Manoharan, *Nature (London)* **483**, 306 (2012).
- [16] L. Tarruell, D. Greif, T. Uehlinger, G. Jotzu, and T. Esslinger, *Nature (London)* **483**, 302 (2012).
- [17] L. Lu, J. D. Joannopoulos, and M. Soljačić, *Nat. Photonics* **8**, 821 (2014).
- [18] T. Jacqmin, I. Carusotto, I. Sagnes, M. Abbarchi, D. D. Solnyshkov, G. Malpuech, E. Galopin, A. Lemaître, J. Bloch, and A. Amo, *Phys. Rev. Lett.* **112**, 116402 (2014).
- [19] S. Wang, D. Scarabelli, Y. Y. Kuznetsova, S. J. Wind, A. Pinczuk, V. Pellegrini, M. J. Manfra, G. C. Gardner, L. N. Pfeiffer, and K. W. West, *Appl. Phys. Lett.* **109**, 113101 (2016).
- [20] L. Nádvořník, M. Orlita, N. A. Goncharuk, L. Smrčka, V. Novák, V. Jurka, K. Hruška, Z. Výborný, Z. R. Wasilewski, M. Potemski *et al.*, *New J. Phys.* **14**, 053002 (2012).
- [21] M. Gibertini, A. Singha, V. Pellegrini, M. Polini, G. Vignale, A. Pinczuk, L. N. Pfeiffer, and K. W. West, *Phys. Rev. B* **79**, 241406(R) (2009).
- [22] A. Singha, M. Gibertini, B. Karmakar, S. Yuan, M. Polini, G. Vignale, M. I. Katsnelson, A. Pinczuk, L. N. Pfeiffer, K. W. West *et al.*, *Science* **332**, 1176 (2011).
- [23] E. Räsänen, C. A. Rozzi, S. Pittalis, and G. Vignale, *Phys. Rev. Lett.* **108**, 246803 (2012).
- [24] I. Kylänpää, M. Aichinger, S. Janecek, and E. Räsänen, *J. Phys.: Condens. Matter* **27**, 425501 (2015).
- [25] I. Kylänpää, F. Berardi, E. Räsänen, P. García-González, C. A. Rozzi, and A. Rubio, *New J. Phys.* **18**, 083014 (2016).
- [26] A. D. Güçlü, P. Potasz, M. Korkusinski, and P. Hawrylak, *Graphene Quantum Dots* (Springer, Berlin, 2014).
- [27] A. D. Güçlü, P. Potasz, and P. Hawrylak, *Phys. Rev. B* **82**, 155445 (2010).
- [28] J. Fernández-Rossier and J. J. Palacios, *Phys. Rev. Lett.* **99**, 177204 (2007).
- [29] W. L. Wang, S. Meng, and E. Kaxiras, *Nano Lett.* **8**, 241 (2008).
- [30] A. D. Güçlü, P. Potasz, O. Voznyy, M. Korkusinski, and P. Hawrylak, *Phys. Rev. Lett.* **103**, 246805 (2009).
- [31] A. D. Güçlü and P. Hawrylak, *Phys. Rev. B* **87**, 035425 (2013).
- [32] F. F. Assaad and I. F. Herbut, *Phys. Rev. X* **3**, 031010 (2013).
- [33] Y. Otsuka, S. Yunoki, and S. Sorella, *Phys. Rev. X* **6**, 011029 (2016).
- [34] P. Buividovich, D. Smith, M. Ulybyshev, and L. von Smekal, *Phys. Rev. B* **99**, 205434 (2019).
- [35] J. Ostmeier, E. Berkowitz, S. Krieg, T. A. Lähde, T. Luu, and C. Urbach, *Phys. Rev. B* **102**, 245105 (2020).
- [36] Y. Saleem, A. Dusko, M. Cygorek, M. Korkusinski, and P. Hawrylak, *Phys. Rev. B* **105**, 205105 (2022).
- [37] A. D. Güçlü, G. S. Jeon, C. J. Umrigar, and J. K. Jain, *Phys. Rev. B* **72**, 205327 (2005).
- [38] C. J. Umrigar, J. Toulouse, C. Filippi, S. Sorella, and R. G. Hennig, *Phys. Rev. Lett.* **98**, 110201 (2007).
- [39] W. M. C. Foulkes, L. Mitas, R. J. Needs, and G. Rajagopal, *Rev. Mod. Phys.* **73**, 33 (2001).
- [40] C. J. Umrigar, M. P. Nightingale, and K. J. Runge, *J. Chem. Phys.* **99**, 2865 (1993).
- [41] A. Ghosal, A. D. Güçlü, C. J. Umrigar, D. Ullmo, and H. U. Baranger, *Nat. Phys.* **2**, 336 (2006).
- [42] A. D. Güçlü, C. J. Umrigar, H. Jiang, and H. U. Baranger, *Phys. Rev. B* **80**, 201302(R) (2009).
- [43] J. Su, M. Telychko, P. Hu, G. Macam, P. Mutombo, H. Zhang, Y. Bao, F. Cheng, Z.-Q. Huang, Z. Qiu *et al.*, *Sci. Adv.* **5**, eaav7717 (2019).
- [44] E. H. Lieb, *Phys. Rev. Lett.* **62**, 1201 (1989).
- [45] C. J. Umrigar, C. Filippi, J. Toulouse, and A. D. Güçlü, CHAMP, a quantum Monte Carlo program, <https://cyrus.lassp.cornell.edu/champ>.